View metadata, citation and similar papers at core.ac.uk

brought to you by CORE

provided by Bern Open Repository and Information System (BORIS)

Elsevier Editorial System(tm) for Earth and Planetary Science Letters
Manuscript Draft

Manuscript Number: EPSL-D-17-00947R2

Title: Unraveling the dynamics of magmatic CO2 degassing at Mammoth Mountain, California

Article Type: Letters

Keywords: CO2 degassing; Mammoth Mountain; numerical modeling; TOUGH2; monitoring

Corresponding Author: Dr. Loic Peiffer, PhD

Corresponding Author's Institution: CICESE

First Author: Loic Peiffer, PhD

Order of Authors: Loic Peiffer, PhD; Christoph Wanner, PhD; Jennifer Lewicki, PhD

Abstract: The accumulation of magmatic CO2 beneath low-permeability barriers may lead to the formation of CO2-rich gas reservoirs within volcanic systems. Such accumulation is often evidenced by high surface CO2 emissions that fluctuate over time. The temporal variability in surface degassing is believed in part to reflect a complex interplay between deep magmatic degassing and the permeability of degassing pathways. A better understanding of the dynamics of CO2 degassing is required to improve monitoring and hazards mitigation in these systems. Owing to the availability of long-term records of CO2 emissions rates and seismicity, Mammoth Mountain in California constitutes an ideal site towards such predictive understanding. Mammoth Mountain is characterized by intense soil CO2 degassing (up to ~1000 t d-1) and tree kill areas that resulted from leakage of CO2 from a CO2-rich gas reservoir located in the upper ~ 4 km. The release of CO2-rich fluids from deeper basaltic intrusions towards the reservoir induces seismicity and potentially reactivates faults connecting the reservoir to the surface. While this conceptual model is well-accepted, there is still a debate whether temporally variable surface CO2 fluxes directly reflect degassing of intrusions or variations in fault permeability. Here, we report the first large-scale numerical model of fluid and heat transport for Mammoth Mountain. We discuss processes (i) leading to the initial formation of the CO2-rich gas reservoir prior to the occurrence of high surface CO2 degassing rates and (ii) controlling current CO2 degassing at the surface. Although the modeling settings are site-specific, the key mechanisms discussed in this study are likely at play at other volcanic systems hosting CO2-rich gas reservoirs. In particular, our model results illustrate the role of convection in stripping a CO2-rich gas phase from a rising hydrothermal fluid and leading to an accumulation of a large mass of CO2 (~107-108 tons) in a shallow gas reservoir. Moreover, we show that both, short-lived (months to years) and long-lived (hundreds of years) events of magmatic fluid injection can lead to critical pressures within the reservoir and potentially trigger fault reactivation. Our sensitivity analysis suggests that observed temporal fluctuations in surface degassing are only indirectly controlled by variations in

source: https://doi.org/10.7892/boris.108615 | downloaded: 24.10.2019

magmatic degassing and are mainly the result of temporally variable fault permeability. Finally, we suggest that long-term CO_2 emission monitoring, seismic tomography and coupled thermal-hydraulic-mechanical modeling are important for CO_2-related hazard mitigation.

*Manuscript
Click here to view linked References

Unraveling the dynamics of magmatic CO_2 degassing at Mammoth Mountain, California

Loïc Peiffer[1*], Christoph Wanner[2], Jennifer L. Lewicki[3]

1. Departamento de Geología, CICESE, Ensenada, B.C., Mexico
2. Institute of Geological Sciences, University of Bern, Bern, Switzerland
3. U.S. Geological Survey, Menlo Park, CA, USA

*Corresponding author: Loïc Peiffer, Departamento de Geología, CICESE, Ensenada, B.C., Mexico (peiffer@cicese.mx)

Abstract

The accumulation of magmatic CO_2 beneath low-permeability barriers may lead to the formation of CO_2-rich gas reservoirs within volcanic systems. Such accumulation is often evidenced by high surface CO_2 emissions that fluctuate over time. The temporal variability in surface degassing is believed in part to reflect a complex interplay between deep magmatic degassing and the permeability of degassing pathways. A better understanding of the dynamics of CO_2 degassing is required to improve monitoring and hazards mitigation in these systems. Owing to the availability of long-term records of CO_2 emissions rates and seismicity, Mammoth Mountain in California constitutes an ideal site towards such predictive understanding. Mammoth Mountain is characterized by intense soil CO_2 degassing (up to ~1000 t d^{-1}) and tree kill areas that resulted from leakage of CO_2 from a CO_2-rich gas reservoir located in the upper ~ 4 km. The release of CO_2-rich fluids from deeper basaltic intrusions towards the reservoir induces seismicity and potentially reactivates faults connecting the reservoir to the surface. While this conceptual model is well-accepted, there is still a debate whether temporally variable surface CO_2 fluxes directly reflect degassing of intrusions or variations in fault permeability. Here, we report the first large-scale numerical model of fluid and heat transport for Mammoth Mountain. We discuss processes (i) leading to the initial formation of the CO_2-rich gas reservoir prior to the occurrence of high surface CO_2 degassing rates and (ii) controlling current CO_2 degassing at the surface. Although the modeling settings are site-specific, the key mechanisms discussed in this study are likely at play at other volcanic systems hosting CO_2-rich gas reservoirs. In particular, our model results illustrate the role of convection in stripping a CO_2-rich gas phase from a rising hydrothermal fluid and leading to an accumulation of a large mass of CO_2 (~10^7-10^8 tons) in a shallow gas reservoir. Moreover, we show that both, short-lived (months to years) and long-lived (hundreds of years) events of magmatic fluid injection can lead to critical pressures within the reservoir and potentially trigger fault reactivation. Our sensitivity analysis suggests that observed temporal fluctuations in surface degassing are only indirectly controlled by variations in magmatic degassing and are mainly the result of temporally variable fault permeability. Finally, we suggest that long-term CO_2 emission monitoring, seismic tomography and coupled thermal-hydraulic-mechanical modeling are important for CO_2-related hazard mitigation.

Keywords: CO_2 degassing, Mammoth Mountain, numerical modeling, TOUGH2, monitoring

1. Introduction

Globally, temporal variations in diffuse volcanic CO_2 emissions have been attributed to mechanisms such as magma and/or magmatic fluid injection, change in crustal permeability and meteorological forcing (e.g., Rogie et al., 2001; Hernandez et al., 2001; Granieri et al., 2010; Arpa et al., 2013; Melian et al., 2014; Lewicki et al., 2014; Werner et al., 2014). In the particular case where volcanic systems host large volumes of CO_2-rich gas beneath low-permeability barriers (e.g. Albani Hills and Latera Caldera, Italy; Dieng Volcanic complex, Indonesia; Mammoth Mountain, USA), temporal variations in CO_2 emissions may result from a complex, yet poorly understood interplay between injection of magmatic CO_2 from below and the permeability of faults controlling CO_2 migration from the reservoir to the surface (e.g., Allard et al., 1989; Annunziatellis et al., 2008; Carapezza et al., 2012; Lewicki et al., 2014; Werner et al., 2014). Accumulation of CO_2 in the near surface may cause vegetation stress and the death of animals (Carapezza et al., 2012; Beaubien et al., 2008). Human fatalities have also been reported, for example, at Mammoth Mountain, California (Hill, 2000), Lakes Monoun and Nyos, Cameroun (Sigurdson, 1987; Tazieff, 1989; Giggenbach et al., 1991), and Dieng Volcanic Complex, Indonesia (Allard et al., 1989). A predictive understanding of volcanic CO_2 emissions is therefore fundamental to develop adequate monitoring strategies. Over the past decades, numerical modeling of fluid and heat transport has evolved towards such a predictive tool and numerous applications to volcanic systems are found in the literature (e.g. Hurwitz et al., 2003; Costa et al., 2008; Ingebritsen et al., 2010; Todesco et al., 2010; Chiodini et al., 2016). The number of modeling studies simulating episodic CO_2-dominated degassing at volcanic systems, however, is still limited and the general understanding of such systems is solely based on a qualitative conceptual model involving the presence of CO_2-rich gas reservoirs or pockets in the subsurface (Giggenbach et al., 1991).

Here we present a numerical modeling study of the dynamics of magmatic CO_2 degassing at Mammoth Mountain (California). Owing to the availability of long-term records of CO_2 emissions rates and seismicity (Werner et al., 2014 and references therein), Mammoth Mountain constitutes an ideal site for gaining more quantitative insight into the CO_2 degassing dynamics of volcanic systems. In particular, we evaluate the processes that (i) favor the formation of large scale CO_2-rich gas reservoirs within the shallow subsurface, and (ii) subsequently control CO_2 emission rates at the surface. Moreover, we discuss the implications of our results in terms of volcanic monitoring and hazard mitigation.

2. Site description

Mammoth Mountain is a dacitic volcano located on the southwestern rim of the Long Valley caldera in California (Fig. 1a). In 1989, Mammoth Mountain transitioned to a state of unrest marked by an 11 month-long low-magnitude ($M \leq 3$) seismic swarm and the onset of intense non-thermal (i.e., cold) CO_2 soil degassing. This led to the formation of areas of tree kill on the volcano flanks, amongst which the Horseshoe Lake tree kill (HSL) is the largest (0.28 km^2) (e.g., Hill and Prejean, 2005). Over the next two decades, further swarms (e.g., 1997, 2006, 2008, 2009, 2011, 2014) occurred and surface degassing fluctuated significantly. Interestingly, CO_2 degassing maxima occurred two to three years after the onset of the 1989, 1997 and 2009 swarms (Fig. 1b).

The conceptual model for explaining such long-term degassing involves a laterally extensive, shallow (<5 km) CO_2-rich gas reservoir, which is overlain by a low-permeability caprock or zone of hydrothermal alteration (Sorey et al., 1998). Gas geothermometry predicts a gas reservoir temperature of ~150 °C (Sorey et al., 1998). Furthermore, a liquid dominated hydrothermal system was postulated to occur beneath the gas reservoir (Sorey et al., 1998). The origin of CO_2 in the reservoir is attributed to the long-term degassing of basaltic intrusions at greater depth (> 10 km), while the observed seismicity is believed to reflect increases in pore pressure associated with the episodic migration of CO_2 from the magmatic intrusion towards the shallow reservoir and the surface. Using a model linking pore geometry and fluid compressibility to Vp/Vs ratios (Takei, 2002), Dawson et al. (2016) estimated the total mass of CO_2 within the shallow gas reservoir as 4.6×10^6 to 1.9×10^8 tons (t).

Although short-term (month-to-month) variations in observed CO_2 emissions at HSL were attributed in part to meteorological forcing, Werner et al. (2014) assumed that the long-term (inter-annual) variations (Fig. 1b) largely reflected deep processes. However, there is still a debate regarding the controls on the observed variation in CO_2 emission rates. On the one hand, Werner et al. (2014) suggested that these oscillations reflect pressurization events caused by changes in the intensity of the magmatic CO_2 input to the reservoir. They excluded the possibility that CO_2 flux oscillations were directly related to changes in permeability of the faults connecting the reservoir to the tree-kill areas. Accordingly, the time lag between major seismic events and maximum surface degassing corresponds to the time required for the CO_2-saturated fluid to ascend from the reservoir to the surface. On the other hand, Lewicki et al. (2014) invoked a permeability control to explain why certain seismic swarms (e.g., 1989, 2009) were followed by an initial increase and subsequent decrease in surface CO_2 emissions, while others (e.g., 2006, 2008) were not. They proposed that if a critical pressure threshold within the reservoir is exceeded, mechanical stress causes the reactivation of existing and/or the opening of new fractures or faults (e.g., Rutqvist et al., 2007), thus increasing the permeability of the stressed rock. Subsequent mineral precipitation and fault strengthening ('fault healing') have the potential to progressively decrease the fracture/fault permeability over time (Gratier, 2011). Variations in permeabilities of degassing pathways hence form an alternative explanation for the observed fluctuations of the CO_2 degassing rate.

3. Numerical model

3.1. Numerical simulator and model mesh

Simulations were performed with TOUGH2 (Pruess et al., 1999), a well-established code for modeling mass and heat flow in volcanic and geothermal systems (Chiodini et al., 2003; Rinaldi et al., 2010; Todesco et al., 2010). Thermophysical properties are provided by the equation of state module ECO2N V2.0 (Pan et al., 2016).

Given the lack of structural information at depth, our model considers an idealized 2D cross-section extending laterally over 6 km from south of Horseshoe Lake to north-west of Mammoth Mountain fumarole (Figs. 1a and 2). The model geometry is based on: (i) the Sorey et al. (1998) schematic cross-section, and (ii) recent seismic tomography studies (Lin, 2013; Dawson et al., 2016). Lin (2013) reinvestigated the 1989-1990 seismic events and located the gas reservoir at a depth of 2-3.5 km. The reservoir depth was confirmed by Dawson et al (2016) who analyzed recent seismic events (2011-2013) while using a different velocity model, although the new study proposes a slightly larger reservoir extent ranging from 0.5–4.5 km depth. Accordingly, the vertical extent of the mesh is set to 3.5 km (depth; z-axis). The model width (E-W direction; y-axis) is 500 m, which includes the extent of the HSL area across the N-S profile. Considering that the reservoir extends ~2.5 km horizontally on a perpendicular cross-section (Lin, 2013), we simulate about a fifth of the actual reservoir volume. Consequently, we consider a fifth of the total CO_2 mass estimated by Dawson et al. (2016) (a "scaled value" of 9.2×10^5 – 3.8×10^7 t) for the gas reservoir in order to constrain our simulations.

The mesh is divided into 4 domains: (i) reservoir, (ii) reservoir seal , (iii) shallow aquifer, and (iv) a fault domain, which connects the reservoir to the HSL area (Fig. 2). The fault zone is simplified to only represent the permeable damage zone, with a width of 20 m, in accordance with field observations worldwide (meters to hundreds of meters; Sibson, 2003). In order to identify the main parameters controlling surface CO_2 degassing at the best-characterized site on Mammoth Mountain, we only model degassing at HSL. Based on the altitude at which springs discharge on the lower volcano flanks and on water table measurements in domestic wells (Evans et al., 2002), we assume that (i) the shallow aquifer appears at the base of the volcanic edifice, roughly at the altitude of HSL, while vertically extending down to the reservoir seal, and (ii) the upper part of the volcano is largely water unsaturated (i.e., filled with air/CO_2). Because pressure gradients induced by an unsaturated porous medium are negligible and topographic load does not affect its pore pressure, we consider atmospheric pressure conditions at the base of the edifice and we do not include the upper part of the volcanic edifice in our model (gray area, Fig. 2). Accordingly, we simulate a flat surface topography. The fault-zone connecting the reservoir to the HSL area is vertical although we do not know the actual geometry. The geometry of the reservoir seal is cone-shaped with an arbitrary thickness varying between 300 and 800 m. Furthermore, the low angle (~10°) of the cone-shaped reservoir boundary allows us to simulate the formation of the proposed large-scale CO_2-rich gas reservoir. With these specifications, the reservoir ranges from a minimum depth of 1.5-2 km down to the lower model boundary at 3.5 km depth, which is in accordance with Lin (2013). Dawson et al. (2016) proposed that the gas reservoir could extend to shallower depths (ca. 0.5 km). While we do not negate this possibility, we chose the Lin (2013) depth range because it is in agreement with the inferred temperature of the CO_2-rich gas reservoir (150 °C, Sorey et al., 1998) and a more conservative geothermal gradient of ~70 °C/km.

3.2. Initial and boundary conditions

At the upper model boundary, the temperature and pressure were fixed to 1 bar and 10 °C, respectively (Fig. 2). Initially, a hydrostatic pressure distribution and a conductive geothermal gradient of ~70°C/km were defined throughout the whole model domain to reach the proposed 150 °C at the top of the reservoir domain. The temperature and pressure obtained for the lower boundary (T = 250°C; P = 320 bar) were fixed throughout all our simulations. The upper boundary was open to fluid and heat flow, while lateral boundaries were heat conductive but impermeable to fluid flow. The lower boundary was divided into 3 different sections (LB1-LB3; Fig. 2) as described below.

Owing to the lack of available data, permeability and other rock properties were defined based on preliminary calibration simulations or were chosen based on related modeling studies (Table 1 and references therein). In particular, a permeability of 10^{-14} m^2 was defined for the reservoir domain because it allows the simulation of convective fluid flow, while a value of 10^{-20} m^2 was defined for the reservoir seal to generate an impermeable formation favoring the development of an overpressured reservoir ($P_{reservoir} > P_{hydrostatic}$). The permeability of the shallow aquifer was set to a moderate value of 5 x 10^{-16} m^2 in order to focus fluid flow along the fault domain and to limit lateral gas migration as suggested by the vertical alignment of shallow (< 2.5 km depth) hypocenters associated with the 1989 swarm (Lin, 2013). The permeability of the area around the upper section of the fault-zone (Fig. 2) was set to that of the fault zone to allow gas to spread laterally in the shallow subsurface and to mimic the surface CO_2 degassing pattern at HSL. The permeability of the fault domain and the lower boundary were varied for different simulation scenarios. The porosity was set to 0.01 for all domains. Values of additional rock properties (density, heat conductivity, specific heat) are provided in Table 1.

4. Simulated scenarios

4.1. Initial gas reservoir formation (A simulations)

We first investigate the initial formation of a large CO_2-rich gas reservoir prior to the occurrence of high surface CO_2 degassing rates by modeling upflow and accumulation of a CO_2-rich fluid into an initially water-saturated reservoir (A simulations; Table 2). To do so, the fault was sealed (k = 1 x 10^{-20} m^2) to impede any fluid flow to the surface. Upflow was induced by injecting a CO_2-rich fluid, further referred to as the 'injection fluid', at a given rate through the bottom of the reservoir (LB1, Fig. 2). Simulated fluid injection lasted 2,000 years to reach a fifth of the CO_2 mass estimated by Dawson et al. (2016) within the reservoir. Under the modeled P-T conditions of the reservoir, the CO_2-rich phase corresponds to supercritical CO_2 with a minor H_2O component (Pan et al., 2016). For simplicity, however, we exclusively use the term 'gas phase'.

An observation from preliminary simulations was that the permeability of the reservoir boundaries is one of the key factors to allow the formation of a free gas-phase within the reservoir. We therefore sealed the lateral boundaries to avoid lateral fluid migration and to accumulate gas over the full reservoir height. Simulating a laterally isolated reservoir is well supported by chemical and isotopic compositions of surface gas samples (e.g. $CO_2/^3He$, $\delta^{13}C_{CO2}$, N_2/Ar, $\delta^{15}N_{N2}$) that are distinct from fluid compositions of the adjacent Long Valley hydrothermal system (Sorey et al., 1998). However, if the reservoir is fully sealed and entirely liquid-saturated when injection starts, the reservoir pressure increases due to the low compressibility of liquid water. Consequently, CO_2 becomes highly soluble and no free gas phase can form. In order to obtain a persistent gas phase within the reservoir, the pressure of the reservoir was limited by allowing fluid circulation across the portion of the lower model boundary surrounding the injection area at LB1 (LB2 and LB3).

In addition to the permeability of the reservoir boundaries, the formation of a free gas phase depends on the dissolved CO_2 content of the injection fluid as well as the fluid injection rate. This is because the CO_2 content dictates whether the injection fluid corresponds to a single-phase liquid or a two-phase liquid-gas mixture (Peiffer et al., 2015). According to

Giggenbach et al. (1991), CO_2 released from magmatic intrusions dissolves in overlying liquid-dominated hydrothermal systems, where the dissolved CO_2 content is buffered by water-rock interaction reactions. Upon migration to shallower depths, CO_2 exsolves in response to the drop in pressure and temperature and may eventually accumulate if the hydrothermal system is overlain by a low-permeability caprock. At Mammoth Mountain, magmatic CO_2 degassing and convection rates are unknown. Hence, we have little information on the dissolved CO_2 content and injection rate into the simulated reservoir (Fig. 2), whether the fluid enters the modeled reservoir in a single or a two-phase state, and how fluid injection into the reservoir and surface CO_2 degassing are linked. The specified time-averaged CO_2 injection rate of 150 t d^{-1} in simulations A (Table 2) should therefore be regarded as a somewhat arbitrary injection rate although it is constrained by the average surface CO_2 degassing rate at HSL over the last decades (Werner et al., 2014). A H_2O injection rate of 1111 t d^{-1} was additionally specified (simulations A1 and A2; Table 2) to simulate a CO_2 content for the injection fluid of 5.2 mol %, which is similar to CO_2 concentrations proposed for buffered hydrothermal systems situated above magmatic intrusions (< 10 mol %; Giggenbach et al., 1991). Moreover, a CO_2 concentration of 5.2 mol % is above the CO_2 solubility under the initial P-T conditions at the lower boundary (4.4 mol % at 320 bar and 250°C). Hence, with the specified injection rates, we initiated the simulations with a two-phase fluid injection, which means that boiling occurs at greater depth than the modeled lower boundary (< 3.5 km depth). While the injected CO_2 is considered to be magmatic (Farrar et al., 1995), the specified H_2O injection corresponds to hydrothermal water that is driven upward together with the CO_2-rich magmatic gas phase (Giggenbach et al., 1991).

Gas accumulation and pressure build-up within the reservoir were explicitly simulated for a moderate (simulation A1; k_{LB2} = k_{LB3} = 10^{-16} m^2) and a low permeability (simulation A2; k_{LB2} = 10^{-18} m^2, k_{LB3} = 10^{-20} m^2) of the lower model boundary. The evolution of the gas saturation (Sg) and liquid/gas velocity vectors for these simulations are shown in Figure 3, while Figure 4 illustrates the corresponding evolution of the gas mass in the reservoir and CO_2 outflow rate across the lower boundary, as well as the final P-T distribution. In the case of a moderately permeable lower model boundary (simulation A1) the injected two-phase fluid separates into a CO_2-rich gas phase and a liquid aqueous phase below the lower model boundary (Figs. 3a-b). Subsequently, the CO_2-rich gas phase flows convectively to the upper part of the reservoir where it accumulates beneath the reservoir seal. In contrast, the liquid phase escapes the lower model domain, which physically corresponds to fluid migration towards a lower section of the reservoir that was not modeled in this study. Such phase separation and subsequent gas accumulation is observed because the permeability of the lower model boundary is high enough to limit the pressure in the reservoir (Fig. 4c), which keeps the CO_2 content of the injection fluid above saturation. It follows that the gas phase progressively fills the entire reservoir domain as illustrated by the continuous increase of the CO_2 mass over time (Fig. 4a). At the end of the simulated 2000-year period a value of 1.5 x 10^7 t CO_2 is reached, which is on the upper range of the Dawson et al. (2016) estimate (scaled value = 3.8 x 10^7 t).

For a low permeability of the lower model boundary (k_{LB2} = 10^{-18} m^2, k_{LB3} = 10^{-20} m^2, simulation A2) total gas accumulation over 2000 years decreases by a factor of two (7.25 x 10^6 t, Fig. 4a) when compared to the moderate permeability scenario (Fig. 4a), although it is still within the Dawson et al. (2016) scaled range (9.2 x 10^5 - 3.8 x 10^7 t). This is because a decrease in permeability of the lower boundary limits fluid migration towards the lower portion of the reservoir and yields an increase in reservoir pressure and thus CO_2 solubility. The initial two-phase injection fluid therefore transitions to a single-phase liquid state. In this case, boiling occurs within the modeled reservoir, impeding the gas phase to accumulate over the full height of the reservoir. Therefore, the lower section of the modeled reservoir remains liquid-dominated (Fig. 3c).

At the top of the CO_2-rich gas reservoir the pressure in the two permeability scenarios differs by 105 bar (Fig. 4c). Hereafter, we refer to the reservoir pressure states in the two simulation scenarios as highly (simulations A2, low permeability) and mildly (simulation A1, moderate permeability) overpressured. In contrast, the temperature profiles for the two scenarios are very similar (Fig. 4c). Likewise, the average CO_2 concentration within the gas-dominated section of the reservoir is not sensitive to lower-boundary permeability and is around 90 mol % at 2,000 years.

Figure 4b shows that most of the injected CO_2 flows downward across the lower model boundary in the dissolved state (hereafter referred to as the 'LB outflow'), while only a limited fraction accumulates as a gas phase in the reservoir. After an initial time period, the ratio between the LB outflow and the CO_2 injection rate within the reservoir (Fig. 4b) has evolved to a steady state, which is not sensitive to the permeability of the lower model boundary. This is why at steady state simulations A1 and A2 are characterized by very similar CO_2 accumulation rates ($\alpha' = 8.8$ t d^{-1}, $\beta = 10.5$ t d^{-1}; Fig .4a). In the supplementary information section 1 we further show that the CO_2 accumulation rate, CO_2 mass and P-T distribution at steady-state are insensitive to the CO_2 concentration of the injection fluid.

4.2. Surface CO_2 degassing

The goals of the second set of simulations were to investigate CO_2 release from the reservoir towards the surface at HSL and to better understand observed variations in surface CO_2 emissions. As such, we conducted two types of simulations to assess the hypotheses that variations in CO_2 input into the reservoir (Werner et al., 2014) versus fault permeability (Lewicki et al., 2014) exerted primary control over surface CO_2 emissions at HSL.

4.2.1. Degassing through a fault with constant permeability (simulations B, C)

To test the effect of reservoir pressure variations on surface CO_2 emission rates, we kept the permeability of the fault constant over time. The B simulations evaluate the loss of CO_2 from the reservoir through the fault zone, assuming a constant magmatic CO_2 injection rate into the reservoir over a period of 30 years. Initial and boundary conditions were taken from the end of simulations A1 and A2 to assess the effect of different initial gas masses and reservoir pressures. The effects of different fault permeabilities ($k_f = 5 \times 10^{-15} - 2 \times 10^{-14}$ m^2) that are held constant over time are investigated through simulations B1-B4 (Table 2). The specified permeability values were all within the range estimated for transient permeability increase associated with fluid migration at Mammoth Mountain ($10^{-14.4} – 10^{-13.9}$ m^2, Ingebritsen and Manning, 2010). Hence, by considering such elevated permeability, these simulations correspond to an end-member scenario where the fault is constantly permeable to fluid flow. Moreover, it should be noted that the fault connecting the reservoir to the surface was initially fully water saturated, which means that the type B simulations model the 'initial' CO_2 loss from a newly formed reservoir (Table 2). In simulations B1-B4, CO_2 reaches the surface after 0.5–3 years, corresponding to the time needed to advectively transport the gas phase along the initially water-saturated fault (Fig. 5a). Interestingly, simulated surface CO_2 emission rates progressively increase over the simulated period of time, and do not oscillate. This is because a large gas mass reservoir cannot be completely depleted over a short period of time. For instance, the CO_2 mass reached at the end of simulation A1 (1.5×10^7 t) would be fully depleted after 274 years considering a constant surface degassing rate of 150 t d^{-1} and the absence of magmatic CO_2 input. The surface CO_2 emission rates are positively correlated with both the fault zone permeability and initial reservoir pressure (Fig. 5a).

The only circumstances under which we observe a decrease in surface CO_2 emission rate with a temporally constant fault permeability and constant magmatic CO_2 influx into the reservoir is when the gas mass in the initially formed reservoir is close to the lower estimate of Dawson et al. (2016) (scaled value: 9.2×10^5 t, Fig. 5a). For instance, a low initial value of 1.63×10^6 t is obtained when running simulation A1 for only 120 years (Fig. 3a). Simulation B5 considers such gas mass and a high permeability of 10^{-13} m^2 for the fault zone as initial conditions. After degassing over 30 years, the gas phase becomes mainly restricted to the upper 350 m of the reservoir (Fig. 6). Because this is shallower than the intersection of the fault zone with the reservoir (Fig. 6) the surface CO_2 emission rate declines sharply over time as observed at HSL after the 1997 and 2009 seismic swarms (Fig. 5a). In the supplementary information section 2 we also show that varying fault location (and thus where the fault intersects the CO_2-rich reservoir) influences the magnitude of CO_2 emissions. The overall temporal pattern in CO_2 emissions, however, is not sensitive to fault location.

Simulations C1-C4 assess the impact of varying the rate of magmatic CO_2 input into the reservoir, while holding the fault permeability constant. To do so, simulations C1 and C2 were initiated by taking the P, T and X_{CO2} distribution as obtained after 10 years of simulation B2. This particular 'restart' time simulates a fault initially saturated with a mixture of gas and liquid (mean Sg = 0.33), and that degases superficially at a rate similar to measured background values at HSL (90 t d^{-1}). Both simulations are run for a period of 20 years. The permeabilities of the lower boundaries at LB2 and LB3 were lowered to 10^{-18} and 10^{-20} m^2, respectively, to obtain a large pressure increase within the reservoir. Simulation C1 starts with a 6-month period of enhanced injection (20 times the rate used for simulations A and B) and continues with the same regular injection rate as in B2 for the remaining time (10.5-30 years). Simulation C2 involves an injection rate that was lowered by a factor of 3 over the entire 20-year period (10-30 years) (Table 2). These two simulations show that varying the rate of magmatic CO_2 input into the reservoir only affects the magnitude of the surface CO_2 emission rate, whereas the temporal degassing patterns remains the same as in simulation B2 (Fig. 5b).

In contrast, simulations C3 and C4 were initiated by taking the physical conditions obtained after 10 years of simulation B5 to simulate the degassing of reservoir with a limited gas mass. An increase in the fluid injection rate by a factor of 20 was imposed for the first 6 months in simulation C3, and for the first three years in simulation C4, while the same injection rate as in B5 was used for the remaining time (Table 2). Under such injection conditions, the pressure gradient within the reservoir increases (Fig. 4c), causing an immediate increase in surface CO_2 emission rates (Fig. 5b). Once the period of enhanced injection stops, the pressure gradient and surface CO_2 emission rates decrease. Maximum CO_2 emission rates are reached at the end of the increased injection period and the degassing evolution is similar to the trend observed at HSL between 1998-2005 and 2009-2013 (Fig. 5b). In fact, setting the period of increased CO_2 injection rate to 3 years results in a relatively close match with the observed pattern in surface CO_2 emissions (simulation C4).

4.2.2. Surface degassing under time-dependent permeability conditions (D simulations)

To investigate the effect of a temporally variable fault permeability on the surface CO_2 degassing rate we kept the initial gas mass within the reservoir and the rate of fluid input constant (150 t d^{-1} CO_2 / 1111 t d^{-1} H_2O, Table 2). By doing so, we test whether a change in fault permeability alone can be responsible for the observed oscillations in surface CO_2 emissions. While we do not explicitly simulate the cause for such permeability variations, they are likely linked to increased fluid injection into the reservoir and subsequent pore pressure increase.

Varying the fault permeability mimics fault zone reactivation and subsequent healing as they likely occur associated with seismic events (Rutqvist et al., 2007). An important consideration for this scenario is that the vertical extent of the fault whose permeability changes is variable. Rinaldi et al. (2014) showed that low-magnitude (M = 2-3.5) seismic events induced by CO_2 injection in carbon capture and storage (CCS) reservoirs do not always cause the reactivation of a fault over its full vertical extent. Therefore, we ran different simulations that varied the permeability of different parts of the fault to test the effect on surface CO_2 degassing. Simulations D1 and D2 consider a temporally variable permeability of the lower fault section (from the reservoir to the top of the reservoir seal), while the permeability of the upper section (from the top of the seal to the surface) remains constant ($k = 2 \times 10^{-14}$ m^2, Table 2). In contrast, simulation D3 considers a temporally variable permeability along the entire vertical extent of the fault.

For each simulation (D1-D3), two cycles of temporally varying fault permeability were carried out to simulate CO_2 degassing under different conditions of fluid saturation within the fault (Fig. 7a). The first cycle (0-5 years) initiates with a fault fully saturated with water (initial conditions inherited from simulation A1), while the second cycle (5-12 years) starts when the system has already been degassing to the surface for a few years and the fault is saturated with a liquid-gas mixture. Simulation D1 is run with a fault permeability that decreases exponentially from 8×10^{-14} to 4×10^{-15} m^2 during 4 years and then remains stable (4×10^{-15} m^2) for the rest of the cycle ($k_f 1$; Fig. 7a). In simulation D2, we apply the same decrease in fault permeability, but over a shorter (3-year) period of time ($k_f 2$, Fig. 7a). Simulation D3 is run with the temporal change in fault permeability following pattern $k_f 1$. The specified exponential permeability decay rate law was taken from published laboratory experiments (Micklethwaite et al., 2016, Table 2). The corresponding permeability decay rates in Table 1 were chosen to match observed surface CO_2 emissions rates, but are consistent with laboratory experiments and field-scale observations (1 order of magnitude over 1–10 years; Ingebritsen and Manning, 2010).

The three D simulations produce different temporal patterns in surface CO_2 emissions (Fig. 7b). As observed for the B simulations, a given time delay is needed to observe degassing at the surface when the fault is initially fully saturated with water. Furthermore, if the entire fault is reactivated (simulation D3) the gas reaches the surface more quickly than in the partial reactivation runs (simulations D1 and D2). In response to the second cycle of permeability variation, simulation D1, and to a lesser extent D2, produce surface CO_2 emission rates that match emission rates measured at HSL (Fig. 7b). The peak in surface CO_2 emission rate is reached ~2-3 years after the instantaneous increase in permeability. Conversely, simulation D3 generates a more intense peak in surface CO_2 emission rate only a few months after the fault is reactivated.

5. Discussion

5.1. Initial formation of a CO_2-rich gas reservoir

Little is known about the rate and temporal pattern of migration of magmatic CO_2 fluids into the shallow crustal reservoir beneath Mammoth Mountain. For an assumed CO_2 injection rate of 150 t d^{-1} our A simulations suggest that the large mass of gas within the reservoir beneath Mammoth Mountain has probably formed over a period of several hundreds of years (Fig. 4a). However, Figure 4a illustrates that the time required for the formation depends on the amount of CO_2 injected to the system and the permeability of the lower boundary. The time required for gas reservoir formation could therefore be much shorter if the CO_2 content of the injection fluid was higher and/or if the lower boundary was more permeable. Conversely, the formation time could be longer if the injection rate is sporadic and lower on average over time. Furthermore, these A simulations illustrate that the accumulation of a large mass of free CO_2 beneath the reservoir seal is only possible if fluid migration occurs towards a lower portion of the reservoir, a process that limits the reservoir pressure over time (Fig. 3). Accordingly, a significant fraction of the CO_2 injected into the reservoir flows downward through the lower model boundary in the dissolved state (Fig. 4b). We propose that the outflowing CO_2-rich fluid forms an isolated, vertical convection cell beneath the gas reservoir. Major lateral outflow, which would be accompanied by groundwater thermal anomalies and mineralized compositions, is unlikely because most springs around Mammoth Mammoth are cold and only weakly mineralized (Evans et al., 2002). A final requirement for forming a large gas mass in the reservoir (as in simulation A1) is that initial boiling of the upflowing CO_2-rich fluid (i.e., CO_2 exsolution) occurs significantly below the reservoir seal and certainly below the lower model boundary at 3.5 km depth. This is because the amount of CO_2 exsolved from a CO_2-rich fluid is maximized if the difference between the P,T conditions at the reservoir top and the P,T-conditions under which initial boiling occurs (i.e., equilibrium P,T for the given CO_2 content) is at its maximum.

5.2. Pathways for CO_2 migration

The spatio-temporal progression of seismicity beneath Mammoth Mountain has been attributed to increases in pore pressure associated with the migration of CO_2-rich magmatic fluids that originate from basaltic intrusions (Hill and Prejean, 2005; Shelly and Hill, 2011; Lewicki et al., 2014; Shelly et al., 2015). According to our simulations, the time required to pressurize the reservoir by an upflowing fluid depends on the reservoir pressure prior to fluid injection into the reservoir, the permeability of the reservoir boundaries, and the rate of magmatic CO_2 influx. Because the location of the tree-kill areas at Mammoth Mountain are consistent with mapped faults (Sorey et al., 1998), it is likely that the maximum overpressure that can be contained within the reservoir is controlled by the presence of such faults (Sibson, 2003). Rutqvist et al. (2007) performed fully coupled thermal-hydraulic-mechanical (THC) simulations of a hypothetical CCS reservoir. Their results showed that rupture of an optimally oriented fault occurs at a critical pressure between 72-84 % of the lithostatic pressure. Simulation C1 suggests that 6 months of enhanced CO_2 injection (20 times the background rate) into a reservoir that is initially mildly overpressured is enough to increase the pressure at the top of the reservoir by 46 bars (Fig. 4c). This yields a pressure that is 74 % of the local lithostatic value. Similar pressures are obtained for long-term but low CO_2 injection rates such as manifested by simulation A2, where the pressure approaches 90% of lithostatic at the reservoir top after 2000 years (Fig. 4c). Even though this comparison with lithostatic pressure is oversimplified, it allows us to conclude that either (i) short-lived events of enhanced CO_2-rich fluid injection or (ii) long-term but low injection rates have the potential to significantly increase the reservoir pressure, trigger fault reactivation and induce high CO_2 emission rates at the surface. The fact that some seismic swarms (e.g., 2006) were not followed by an increase in CO_2 emission rates might indicate that the reservoir pore pressure may not have exceeded the critical value (Fig. 1b; Lewicki et al., 2014).

5.3. Causes of variations in surface CO_2 degassing rates

Our simulations showed that the oscillating CO_2 emission rates observed at HSL could have solely resulted from (i) an increase in fluid injection rate into the reservoir at constant fault permeability (simulation C4, Fig. 5b) or (ii) temporally and spatially variable fault permeability associated with seismicity and subsequent fault healing (simulation D1, Fig. 7b). The former scenario, however, requires that the drainable portion of the CO_2-rich gas reservoir is small, and that the period of enhanced injection is similar to the 2-3 year time lag of the CO_2 degassing peak. Moreover, the continuous surface CO_2 degassing observed at HSL since 1989 (Fig. 1b) suggests that the reservoir gas mass has remained above a certain threshold value. As such, the constant permeability scenario requires a delicate mass balance between magmatic input into the reservoir and surface degassing.

The variable permeability scenario requires us to define specific parameter values to match the degassing pattern at HSL. Simulation results were most sensitive to the length of the fault subjected to permeability variations, the magnitude of the permeability increase and the timing of the subsequent permeability decay. Interestingly, very high CO_2 upflow velocities were observed along the fault after it was partially saturated with gas (e.g. 13 km yr^{-1} at five years in simulations D1). It follows that the time delay of ~2-3 years (Fig. 1b) observed between the occurrence of seismic swarms and the maximum rate of surface CO_2 degassing does not correspond to the time required for the gas to ascend from the reservoir to the surface (2 km flow distance). Rather, it likely reflects the time required for the permeability of the reactivated (i.e., lower) fault section to drop to its initial (pre-reactivation) value (Fig. 7a).

Due to the lack of precisely constrained parameter values (Table 1) our simulations are underconstrained. Accordingly, multiple parameter value combinations can yield to the same degassing behavior and we cannot exclude one of the simulated scenarios. Nevertheless, given the observed spatial and temporal correlations between seismic swarms, fault location and degassing peaks (Fig. 1) it seems rather convincing that permeability variations play a highly important role as suggested by our D simulations.

Although we did not investigate CO_2 degassing in other areas on Mammoth Mountain, $^{4}He/^{3}He$ ratios from MMF and magmatic CO_2 concentration recorded in tree-rings at the Chair 12 tree-kill area suggest similar patterns in degassing behavior (Lewicki et al., 2014; Evans et al., 2011; W.C. Evans, unpublished data). Such observation might indicate that other degassing areas are linked to the reservoir by faults displaying similar behavior.

6. Summary and conclusions

The accumulation of magmatic CO_2 beneath low-permeability barriers may lead to the formation of CO_2-rich gas reservoirs within volcanic systems. CO_2 degassing from such systems can result in human, animal and plant mortality. Owing to the availability of long-term records of CO_2 emissions rates and seismicity, Mammoth Mountain is an ideal site to gain quantitative insight into the dynamics of CO_2 degassing in these volcanic systems.

Here, we present the first large-scale numerical model of fluid and heat transport for Mammoth Mountain. Simulations demonstrated that the occurrence of vertical convection cells is crucial for the formation of a large CO_2-rich gas reservoir because it limits the reservoir pressure and favors exsolution of gaseous CO_2 and accumulation within the reservoir. A subsequent sensitivity analysis assessed whether temporal variations in magmatic CO_2 input into the reservoir or fault permeability exert the primary control on surface degassing. This analysis demonstrated that the scenario in which fault permeability varied does not require a specific gas-reservoir volume or a precise fault location to induce observed oscillations in surface degassing at Mammoth Mountain. Therefore, this scenario offers a more generally applicable explanation. Temporal variations in fault permeability are likely due to (1) increase in pore pressure associated with the migration of magmatic fluids that induces fault reactivation and (2) subsequent fault healing. Although we favor this explanation, variations in magmatic fluid input (with constant fault permeability) may explain observed patterns in surface CO_2 emissions, but only if the drainable portion of the gas reservoir is limited in volume.

Similar degassing dynamics are likely at play at other volcanic systems hosting CO_2-rich gas reservoir beneath low-permeability barriers (e.g. Albani Hills and Latera Caldera, Dieng Volcanic complex). Our findings generally imply that the intensity of CO_2 emissions and the time delay between seismic activity and peaks in surface CO_2 emission rates should not only be interpreted in terms of magmatic degassing, but also in terms of the integrity of the reservoir seal and changes in fault permeability. An implication of the observation that CO_2 emission peaks are not synchronous with periods of increased seismicity is that hazard mitigation should include long-term CO_2 emission monitoring, especially after the occurrence of increased seismicity. Moreover, the fact that CO_2 degassing is strongly controlled by the presence and integrity of the reservoir seal calls for performing detailed seismic tomography to locate such seals. Coupled thermal-hydraulic-mechanical modeling constrained by the local stress regime and fault geometry is required to better define the maximum overpressure that can be contained within the reservoir before fault rupture. Such analyses will allow for improved CO_2 emission monitoring and hazard mitigation, especially with respect to the time lag to be expected between increased seismicity and CO_2 emission peaks.

Acknowledgments

L. Peiffer was supported by the CEMIE-GEO Conacyt-SENER Laboratory project ('Sistema de Laboratorios Especializados') and an internal CICESE project. The Swiss Competence Center for Energy Research – Supply of Electricity (SCCER-SoE) supports research in geothermal energy at the University of Bern. We thank W.C. Evans and three anonymous reviewers for constructive review of the manuscript. We also thank T. Mather for efficient and constructive editorial handling. Any use of trade, firm, or product names is for descriptive purposes only and does not imply endorsement by the U.S. Government. All the data are available upon request to the authors.

References

Allard, P., Dajlevic, D., Delarue, C., 1989. Origin of carbon dioxide emanation from the 1979 Dieng eruption, Indonesia: Implications for the origin of the 1986 Nyos catastrophe. J. Volcanol. Geotherm. Res., 39, 195-206.

Annunziatellis, A., Beaubien, S.E., Bigi, S., Ciotoli, G., Coltella, M., Lombardi, S., 2008. Gas migration along fault systems and through the vadose zone in the Latera caldera (central Italy): Implications for CO_2 geological storage. Int. J. Greenh. Gas Control 2, 353-372.

Arpa, M.C., Hernández, P.A., Padrón, E., Reniva, P., Padilla, G.D., Bariso, E., Melián, G., Barrancos, J., Nolasco, D., Calvo, D., Pérez, N.M., Solidum, R.U.J., 2013. Geochemical evidence of magma intrusion inferred from diffuse CO_2 emissions and fumarole plume chemistry: the 2010–2011 volcanic unrest at Taal Volcano, Philippines. Bull. Volcanol., 75:747, https://doi.org/10.1007/s00445-013-0747-9.

Beaubien, S. E., Ciotoli, G., Coombs, P., Dictor, M. C., Krüger, M., Lombardi, S., Pearce, J.M., West, J. M., 2008. The impact of a naturally occurring CO_2 gas vent on the shallow ecosystem and soil chemistry of a Mediterranean pasture (Latera, Italy). Int.J. Greenh. Gas Con., 2(3), 373-387.

Carapezza, M.L., Barberi, F., Ranaldi, M., Ricci, T., Tarchini, L., Barrancos, J., Fischer, C., Granieri, D., Lucchetti, C., Melian, G., Perez, N., Tuccimei, P., Vogel, A., Weber, K., 2012. Hazardous gas emissions from the flanks of the quiescent Colli Albani volcano (Rome, Italy). Appl. Geochem., 27, 1767-1782.

Chiodini, G., Todesco, M., Caliro, S., Del Gaudio, C., Macedonio, G., Russo, M., 2003. Magma degassing as a trigger of bradyseismic events: The case of Phlegrean Fields (Italy), Geophys. Res. Lett., 30(8), 1434, doi:10.1029/2002GL016790.

Chiodini, G., Caliro, S., Cardellini, C., Granieri, D., Avino, R., Baldini, A., Donnini, M., Minopoli, C., 2010. Long-term variations of the Campi Flegrei, Italy, volcanic system as revealed by the monitoring of hydrothermal activity. J. Geophys. Res. Solid Earth, 115(B3), doi: 10.1029/2008JB006258.

Chiodini, G., Tassi, F., Caliro, S., Chiarabba, C., Vaselli, O., Rouwet, D., 2012. Time-dependent CO_2 variations in Lake Albano associated with seismic activity. Bulletin of volcanology, 74(4), 861-871.

Chiodini, G., Paonita, A., Aiuppa, A., Costa, A., Caliro, S., De Martino, P., Acocella, V., Vandemeulebrouck, J., 2016. Magmas near the critical degassing pressure drive volcanic unrest towards a critical state. Nat. Commun. 7, 13712, doi: 10.1038/ncomms13712.

Costa, A., Chiodini, G., Granieri, D., Folch, A., Hankin, R. K. S., Caliro, S., Avino, R., Cardellini, C., 2008. A shallow-layer model for heavy gas dispersion from natural sources: Application and hazard assessment at Caldara di Manziana, Italy, Geochem. Geophys. Geosyst., 9, Q03002, doi:10.1029/2007GC001762.

Dawson, P., Chouet, B., Pitt, A., 2016. Tomographic image of a seismically active volcano: Mammoth Mountain, California. J. Geophys. Res. Solid Earth, 121, 114-133, doi:10.1002/2015JB012537.

Evans, W. C., Sorey, M. L., Cook, A. C., Kennedy, B. M., Shuster, D. L., Colvard, E. M., White, L. D., Huebner, M. A., 2002. Tracing and quantifying magmatic carbon discharge in cold groundwaters: lessons learned from Mammoth Mountain, USA. J. Volcanol. Geotherm. Res., 114(3), 291-312.

Evans, W.C., Mangan, M., McGeehin, J.P., King, J., Lewicki, J.L., Hilley, G., 2011. Magmatic CO_2 emissions at Mammoth Mountain, California, tracked by ^{14}C in tree core. Abstract V21A-2483 presented at 2011 Fall Meeting, AGU, San Francisco, CA, 5–9Dec.

Granieri, D., Avino, R., Chiodini, G., 2010. Carbon dioxide diffuse emission from the soil: ten years of observations at Vesuvio and Campi Flegrei (Pozzuoli), and linkages with volcanic activity. Bull. Volcanol., 72, 103–118, doi:10.1007/s00445-009-0304-8.

Gratier, J. P., 2011. Fault permeability and strength evolution related to fracturing and healing episodic processes (years to millennia): the role of pressure solution. Oil Gas Sci. Technol. 66 (3), 491-506.

Gruen, G., Weis, P., Driesner, T., Heinrich, C. A., de Ronde, C. E., 2014. Hydrodynamic modeling of magmatic–hydrothermal activity at submarine arc volcanoes, with implications for ore formation. Earth Planet. Sci. Lett., 404, 307-318.

Hernández, P.A., Notsu, K., Salazar, J.M., Mori, T., Natale, G., Okada, H., Virgilli, G., Shimoike, Y., Sato, M., Perez, N.M., 2001. Carbon dioxide degassing by advective flow from Usu volcano, Japan. Science 2001, 83–86.

Hill, P. M., 2000. Possible asphyxiation from carbon dioxide of a cross-country skier in eastern California: a deadly volcanic hazard. Wild. Environ. Med., 11(3), 192-195.

Hill, D.P., Prejean, S., 2005. Magmatic unrest beneath Mammoth Mountain, California. J. Volcanol. Geotherm. Res. 146, 257–283.

Hurwitz, S., K. L. Kipp, S. E. Ingebritsen, Reid, M. E.., 2003. Groundwater flow, heat transport, and water table position within volcanic edifices: Implications for volcanic processes in the Cascade Range, J. Geophys. Res., 108(B12), 2557, doi:10.1029/2003JB002565.

Ingebritsen, S. E., Manning, C. E., 2010. Permeability of the continental crust: dynamic variations inferred from seismicity and metamorphism. Geofluids, 10(1-2), 193-205.

Ingebritsen, S. E., Geiger, S., Hurwitz, S., & Driesner, T., 2010. Numerical simulation of magmatic hydrothermal systems. Rev. Geophys., 48(1), doi: 10.1029/2009RG000287.

Lewicki, J. L., Birkholzer, J., Tsang, C. F., 2007. Natural and industrial analogues for leakage of CO_2 from storage reservoirs: identification of features, events, and processes and lessons learned. Environ. Geol., 52(3), 457.

Lewicki, J. L., Hilley, G. E., Shelly, D. R., King, J. C., McGeehin, J. P., Mangan, M., Evans, W. C., 2014. Crustal migration of CO_2-rich magmatic fluids recorded by tree-ring radiocarbon and seismicity at Mammoth Mountain, CA, USA. Earth Planet. Sci. Lett. 390, 52-58.

Lin, G., 2013. Seismic investigation of magmatic unrest beneath Mammoth Mountain, California, USA. Geology, 41 (8), 847-850.

Manning, C. E., Ingebritsen, S. E., 1999. Permeability of the continental crust: Implications of geothermal data and metamorphic systems, Rev. Geophys., 37, 127–150, doi:10.1029/1998RG900002.

Melián, G., Hernández, P.A., Padrón, E., Pérez, N.M., Barrancos, J., Padilla, G., Dionis, S., Rodríguez, F., Calvo, D., Nolasco, D., 2014. Spatial and temporal variations of diffuse CO_2 degassing at El Hierro volcanic system: Relation to the 2011–2012 submarine eruption. J. Geophys. Res. 119, doi: 10.1002/2014JB011013.

Micklethwaite, S., Ford, A., Witt, W., Sheldon, H.A., 2016. Transient permeability in fault stepovers and rapid rates of orogenic gold deposit formation. In: Gleeson, T., Ingebritsen, S.E. (Eds), Crustal permeability. John Wiley & Sons Ltd, UK, pp. 249-259.

Pan, L., Spycher, N., Doughty, C., Pruess, K., 2016. ECO2N V2.0: A TOUGH2 fluid property module for modeling CO_2-H_2O-NACL systems to elevated temperatures of up to 300° C. Greenh. Gases 7 (2), 313-327.

Peiffer, L., Wanner, C., Pan, L., 2015. Numerical modeling of cold magmatic CO_2 flux measurements for the exploration of hidden geothermal systems. J. Geophys. Res. Solid Earth, 120(10), 6856-6877, doi:10.1002/2015JB012258.

Pruess, K., C. Oldenburg, Moridis, G., 1999. TOUGH2: User's guide, version 2.0 Rep. LBNL-43134, Lawrence Berkeley Natl. Lab., Berkeley, Calif.

Rinaldi, A., Todesco, M., Bonafede, M., 2010. Hydrothermal instability and ground displacement at the Campi Flegrei caldera, Phys. Earth Planet. Inter., 178, 155–161, doi:10.1016/j.pepi.2009.09.005.

Rinaldi, A. P., Rutqvist, J., Cappa, F., 2014. Geomechanical effects on CO_2 leakage through fault zones during large-scale underground injection. Int. J. Greenh. Gas Con., 20, 117-131.

Rogie, J.D., Kerrick, D.M., Sorey, M.L., Chiodini, G., Galloway, D.L., 2001. Dynamics of carbon dioxide emission at Mammoth Mountain, California. Earth Planet. Sci. Lett. 188, 535–541.

Rutqvist, J., Birkholzer, J., Cappa, F., Tang, C. F., 2007. Estimating maximum sustainable injection pressure during geological sequestration of CO_2 using coupled fluid flow and geomechanical fault-slip analysis. Energ. Convers. Manage. 48(6), 1798-1807.

Shelly, D. R., Hill, D. P., 2011. Migrating swarms of brittle-failure earthquakes in the lower crust beneath Mammoth Mountain, California, Geophys. Res. Lett., 38(20), L20307, doi:10.1029/2011GL049336.

Shelly, D.R., Taira, T., Prejean, S.G., Hill, D.P., Dreger, D.S., 2015. Fluid-faulting interactions: Fracture-mesh and fault-valve behavior in the February 2014 Mammoth Mountain, California, earthquake swarm. Geophys. Res. Lett., 42, 5803-5812, doi:10.1002/2015GL064325.

Sibson, R. H., 2003. Thickness of the seismic slip zone. B. Seismol. Soc. Am., 93(3), 1169-1178.

Sigurdsson, H. (1987), Lethal gas bursts from Cameroon Crater Lakes, Eos Trans. AGU, 68(23), 570–573, doi:10.1029/EO068i023p00570-04.

Sorey, M. L., Evans, W. C., Kennedy, B. M., Farrar, C. D., Hainswort, L. J., Hausback, B., 1998. Carbon dioxide and helium emissions from a reservoir of magmatic gas beneath Mammoth Mountain, California, J. Geophys. Res., 103, 15,303–15,323, doi:10.1029/98JB01389.

Takei, Y., 2002. Effect of pore geometry on VP/VS: From equilibrium geometry to crack, J. Geophys. Res., 107(B2), doi:10.1029/2001JB000522.

Tazieff, H., 1989. Mechanisms of the Nyos carbon dioxide disaster and of so-called phreatic steam eruptions. J. Volcanol. Geotherm. Res., 39(2-3), 109-116.

Todesco, M., Rinaldi, A. P. , Bonafede, M., 2010. Modeling of unrest signals in heterogeneous hydrothermal systems, J. Geophys. Res., 115, B09213, doi:10.1029/2010JB007474.

Wanner, C., Peiffer, L., Spycher, N. Sonnenthal, E., Kennedy, B. M., Iovenitti, J., 2014, Reactive transport modeling of the Dixie Valley geothermal area: Insights on flow and geothermometry, Geothermics, 51, 130–141.

Werner, C., D. Bergfeld, M. P. Doukas, C. D. Farrar, P. J. Kelly, Kern, C., 2014, Decadal-scale variability of diffuse CO_2 emissions and seismicity revealed from long-term monitoring (1995–2013) at Mammoth Mountain, California, USA, J. Volcanol. Geotherm. Res., 289, 51–63.

Figure captions

Figure 1. (a) Relief map showing the location of Mammoth Mountain (white line), the Horseshoe Lake tree kill area (HSL) and the Mammoth Mountain fumarole (MMF). The dashed black line corresponds to the location of the Long Valley caldera rim, while the gray line shows the Mammoth Mountain fault trace. The modeled cross-section is represented by the dashed white line. (b) Time series of surface CO_2 emission rate (t d^{-1}) at HSL and number of shallow earthquakes (< 10 km depth) per month (modified from Werner et al., 2014). Arrows show time delays between major seismic events and degassing peaks. Direct measurements of CO_2 emissions were not performed until 1995 (dashed line). The pre-1995 flux data were extrapolated from measurements of steam flux at MMF and considering average steam to CO_2 emission ratio, while post-1995 data correspond to CO_2 emission rates calculated based on direct CO_2 flux measurements using the accumulation chamber method. Error bars associated with post-1995 data correspond to one standard deviation of the mean emissions.

Figure 2. Schematic representation of the 2-D model. Different domains (reservoir, seal, shallow aquifer and fault) are assigned specific permeabilities (k). Other rock properties are: porosity (Φ), density (ρ), thermal conductivity (λ) and specific heat (C_r). The arrow symbolizes the injection a CO_2-rich magmatic fluid through the central portion of the lower boundary (dashed white area; LB1). The grey area corresponding to the volcanic summit is not modeled. Mesh discretization (number of blocks (b) and their extent along x-y-z axes) is also shown. Depth is relative to the topographic base of Mammoth Mountain with a mean altitude of 2,500 m asl.

Figure 3. Gas saturation (Sg) distribution and corresponding liquid (grey) and gas (black) velocity vectors at (a) 120 years of simulation A1, (b) 2000 years of simulation A1, (c) 2000 years of simulation A2.

Figure 4. (a) Temporal evolution of CO_2 gas mass within the simulated reservoir in simulations A1, A2. Slopes α, α', β correspond to the average rates of CO_2 accumulation in the reservoir: $\alpha = 38$ t d^{-1} (computed from 0 to 800 years), $\alpha' = 8.8$ t d^{-1} (from 800 to 2000 years), $\beta = 10.5$ t d^{-1} (from 250 to 2000 years). (b) Corresponding temporal evolution of the outflow rate in dissolved CO_2 through the lower boundaries (LB2 and LB3) as a percentage of the CO_2 injection rate. (c) Pressure and temperature profiles along the mid-mesh vertical axis (x = 3000 m) after 2,000 years of simulation. The grey and black dotted curves show the pressure distribution after 5 years of enhanced injection in simulation C1 and C3 (time = 15 years). The shaded grey area symbolizes the depth of the low-permeability seal.

Figure 5. (a) Temporal evolution of simulated surface CO_2 emission rate considering the effect of reservoir depletion with constant fault permeability (k_f) and magmatic fluid injection rate. (b) Response in surface CO_2 emission rate to an increase or decrease in magmatic fluid injection with constant $k_{f;}$. Ovals indicate the particular time at which simulations C were initiated, as well as the simulations from which initial conditions were inherited. Dotted curves labeled '98-05' and '09-13' refer to surface CO_2 emission rates observed at Horsehoe Lake over the periods 1998-2005 and 2009-2013, respectively (Werner et al., 2014). Major model parameters are synthetized in boxes. Permeability values refer to fault permeabilities.

Figure 6. Gas saturation (Sg) distribution for two selected simulations (B2 and B5) at 30 years. Triangles show the corresponding surface CO_2 emission rate at this time in Figure 5a.

Figure 7: (a) Simulated temporal variations in fault permeability (k_f) following patterns k_f1 and k_f2. Simulations D1 and D3 are run with pattern k_f1 and simulation D2 with patterm k_f2. (b) Times series of simulated surface CO_2 emission rate considering the effect of variations in fault permeability and constant magmatic fluid injection. Sudden increase in permeability occurs at 0 and 5 years to simulate fault reactivation. Emission rate of simulation D3 is on right y-axis. Dotted curves labeled '98-05' and '09-13' refer to surface CO_2 emission rates observed at Horsehoe Lake over the periods 1998-2005 and 2009-2013, respectively (Werner et al., 2014). Maximum emission rate at the surface in simulations D1 and D2 is observed ~2 years after the second event of fault permeability increase.

Table caption

Table 1: Synthesis of specified model parameters and corresponding sources.

Table 2: Parameters of simulated scenarios. k_f is fault permeability. k_{LB2} and k_{LB3} are permeabilities of the lower boundary at LB2 and LB3, respectively. INCON are initial conditions inherited from another simulation at a certain time. L and UP are lower and upper sections of the fault, respectively. The injection rates of 150 t d^{-1} CO_2 and 1111 t d^{-1} H_2O were specified to simulate a CO_2 content for the injection fluid of 5.2 mol %.

Figure 1

a)

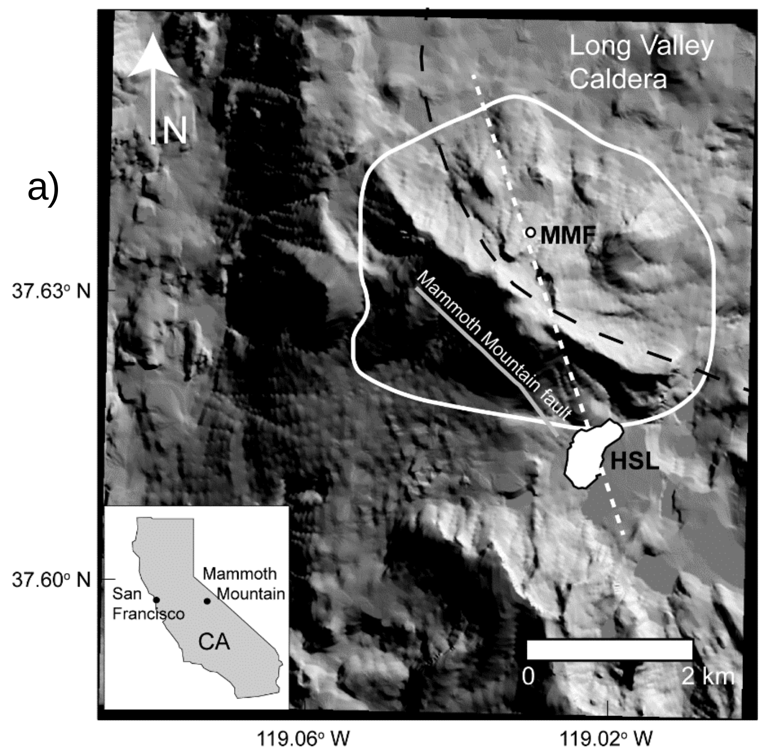

N
Long Valley
Caldera
MMF
Mammoth Mountain fault
HSL
0
2 km
37.63° N
37.60° N
119.06° W
119.02° W
San
Francisco
Mammoth
Mountain
CA

b)

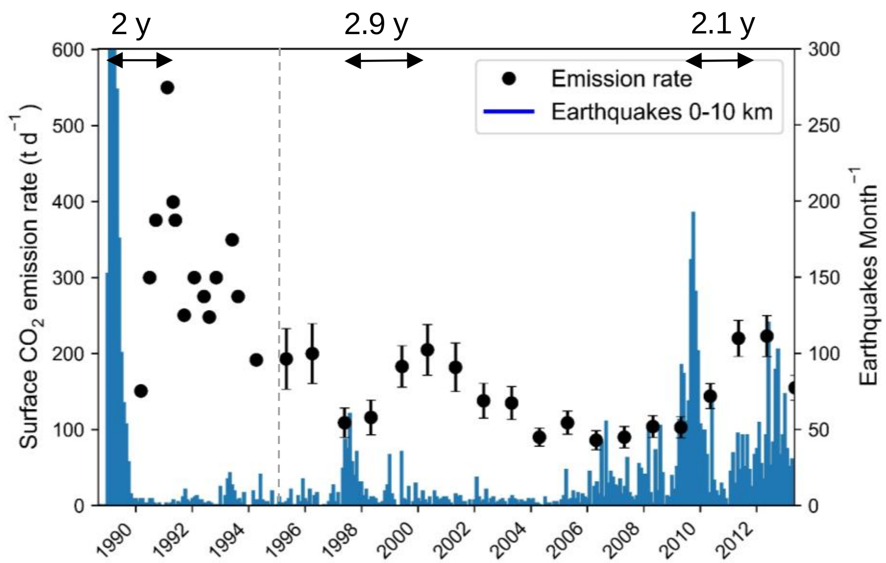

2 y
2.9 y
2.1 y
Emission rate
Earthquakes 0-10 km
Surface CO_2 emission rate (t d^{-1})
Earthquakes $Month^{-1}$
600
500
400
300
200
100
0
300
250
200
150
100
50
0
1990
1992
1994
1996
1998
2000
2002
2004
2006
2008
2010
2012

Figure 2

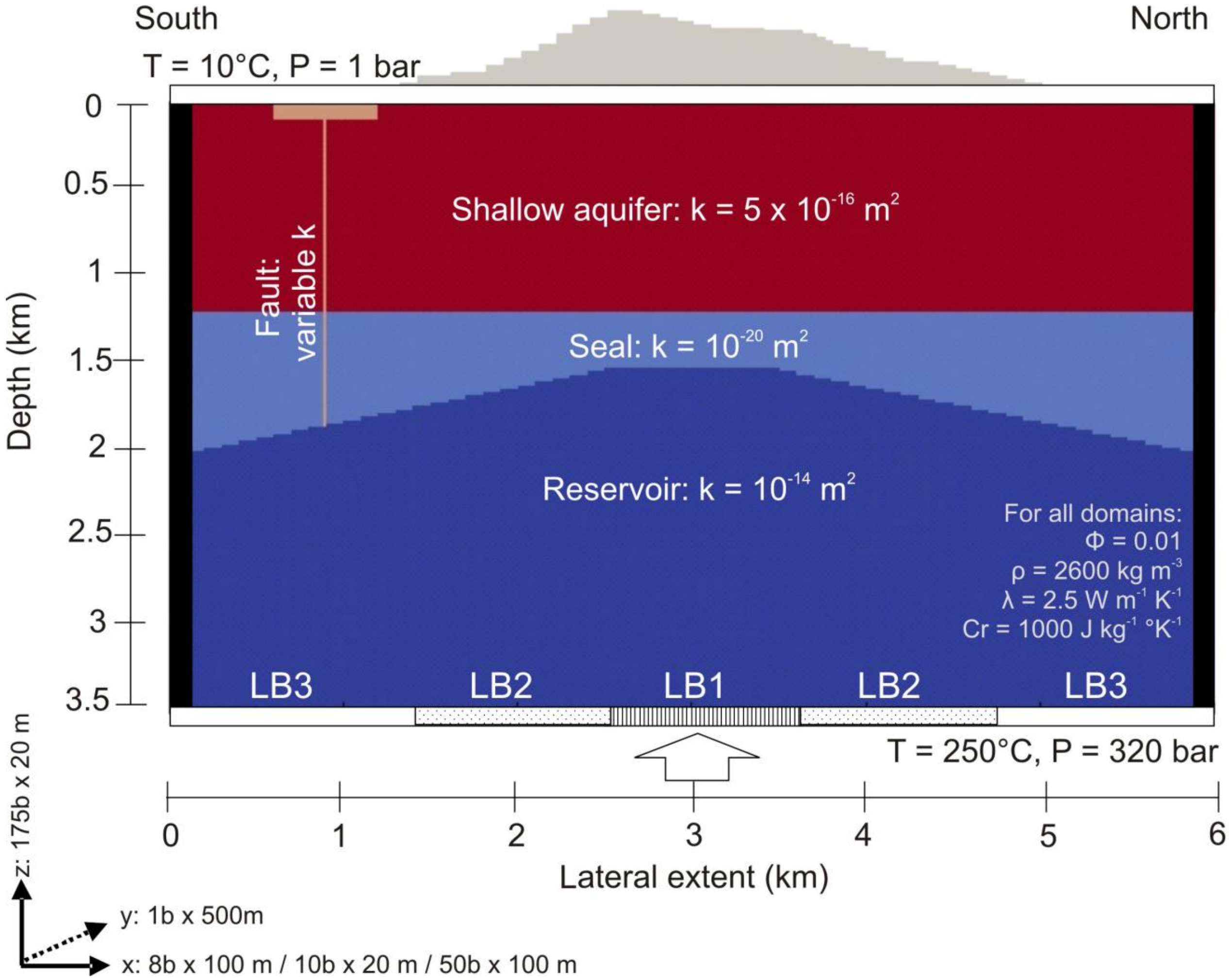

South
North
T = 10°C, P = 1 bar
0
0.5
1
1.5
2
2.5
3
3.5
Depth (km)
Fault: variable k
Shallow aquifer: k = 5 x 10^{-16} m^2
Seal: k = 10^{-20} m^2
Reservoir: k = 10^{-14} m^2
For all domains:
Φ = 0.01
ρ = 2600 kg m^{-3}
λ = 2.5 W m^{-1} K^{-1}
Cr = 1000 J kg^{-1} °K^{-1}
LB3
LB2
LB1
LB2
LB3
T = 250°C, P = 320 bar
0
1
2
3
4
5
6
Lateral extent (km)
z: 175b x 20 m
y: 1b x 500m
x: 8b x 100 m / 10b x 20 m / 50b x 100 m

Figure 3

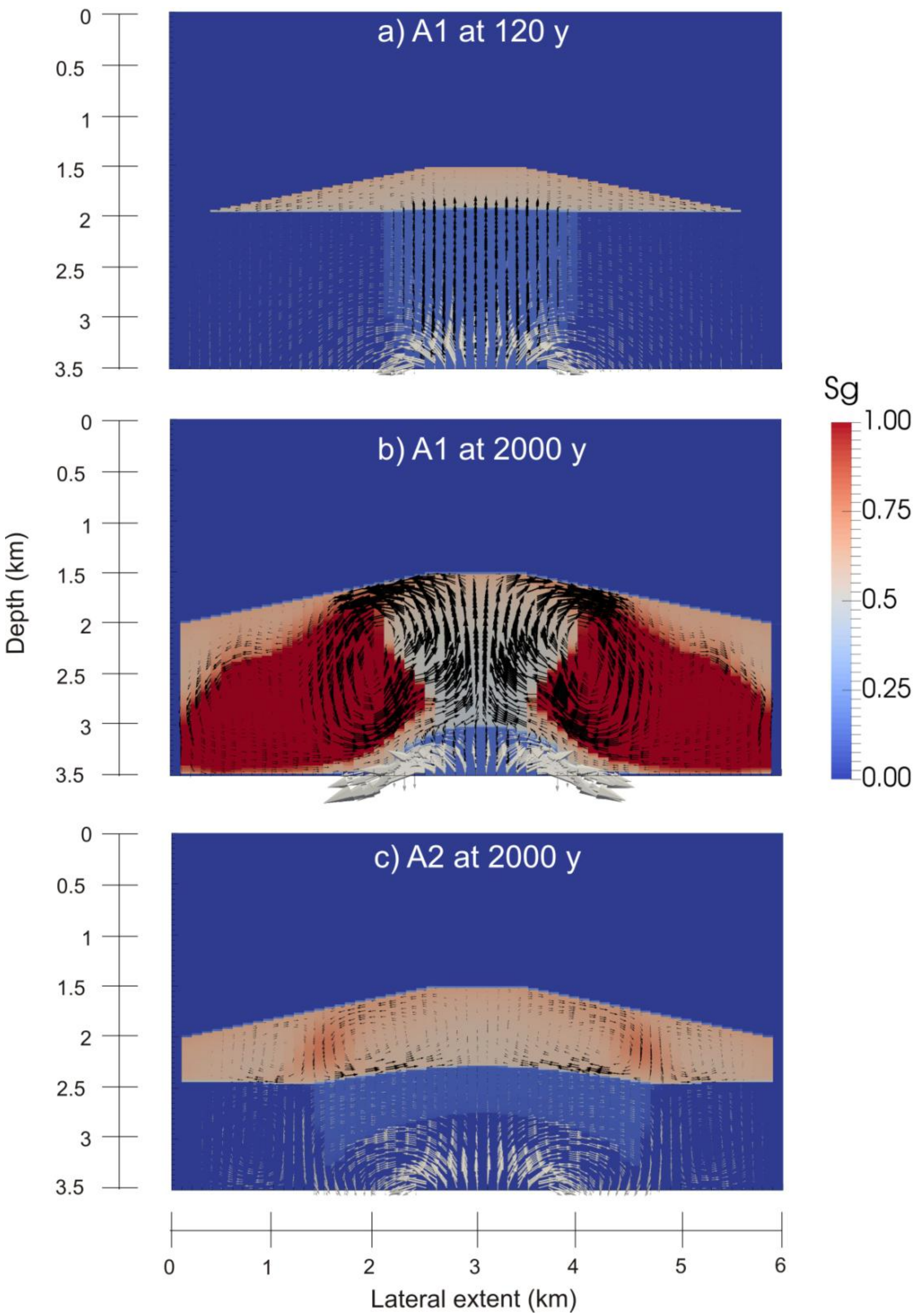

a) A1 at 120 y
b) A1 at 2000 y
c) A2 at 2000 y
Depth (km)
0
0.5
1
1.5
2
2.5
3
3.5
Sg
1.00
0.75
0.5
0.25
0.00
Lateral extent (km)
0
1
2
3
4
5
6

Figure 4

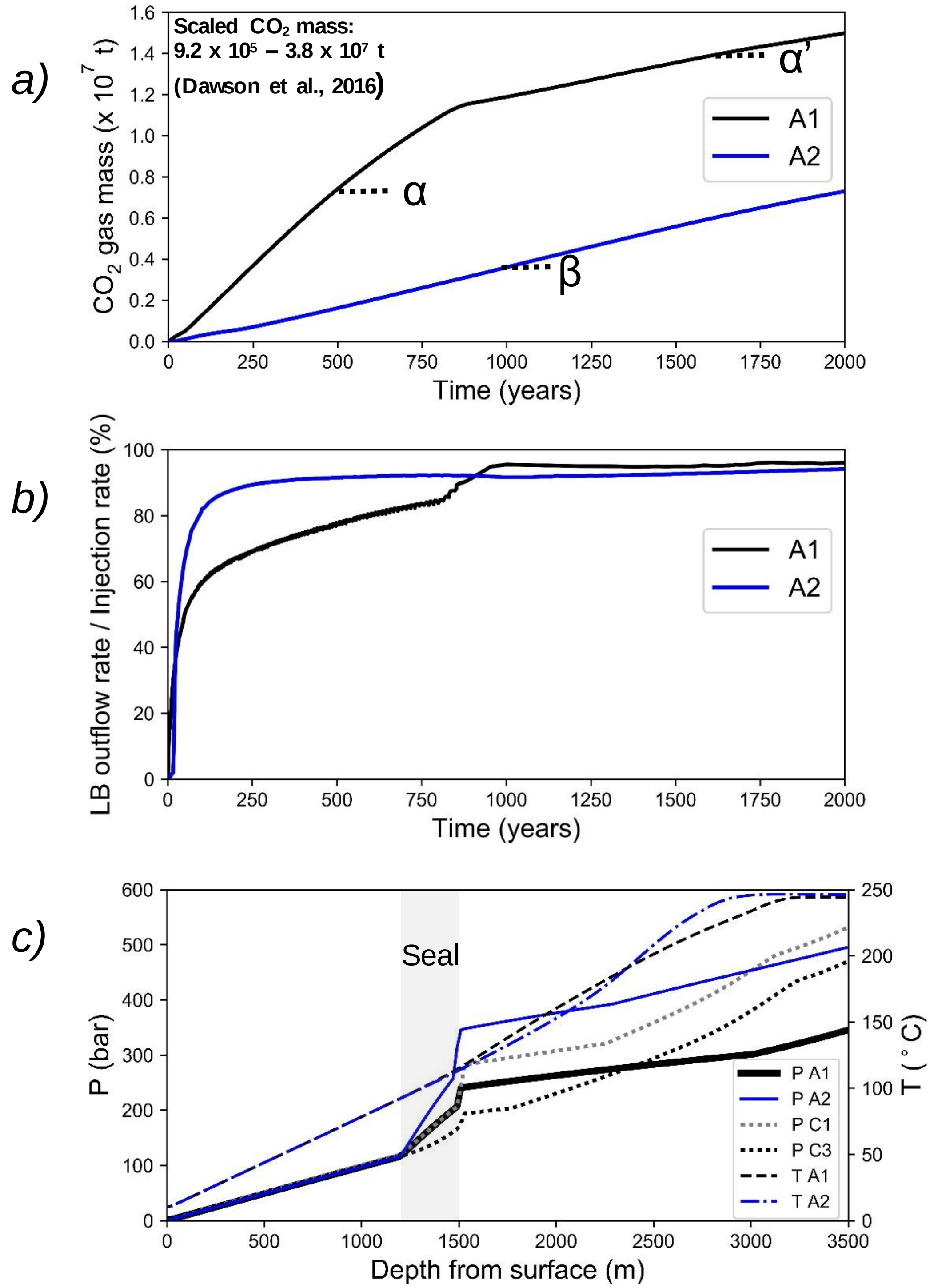
a)
Scaled CO_2 mass:
9.2 x 10^5 – 3.8 x 10^7 t
(Dawson et al., 2016)
CO_2 gas mass (x 10^7 t)
Time (years)
α
α'
β
A1
A2
b)
LB outflow rate / Injection rate (%)
Time (years)
A1
A2
c)
Seal
P (bar)
T (°C)
Depth from surface (m)
P A1
P A2
P C1
P C3
T A1
T A2

Figure 5

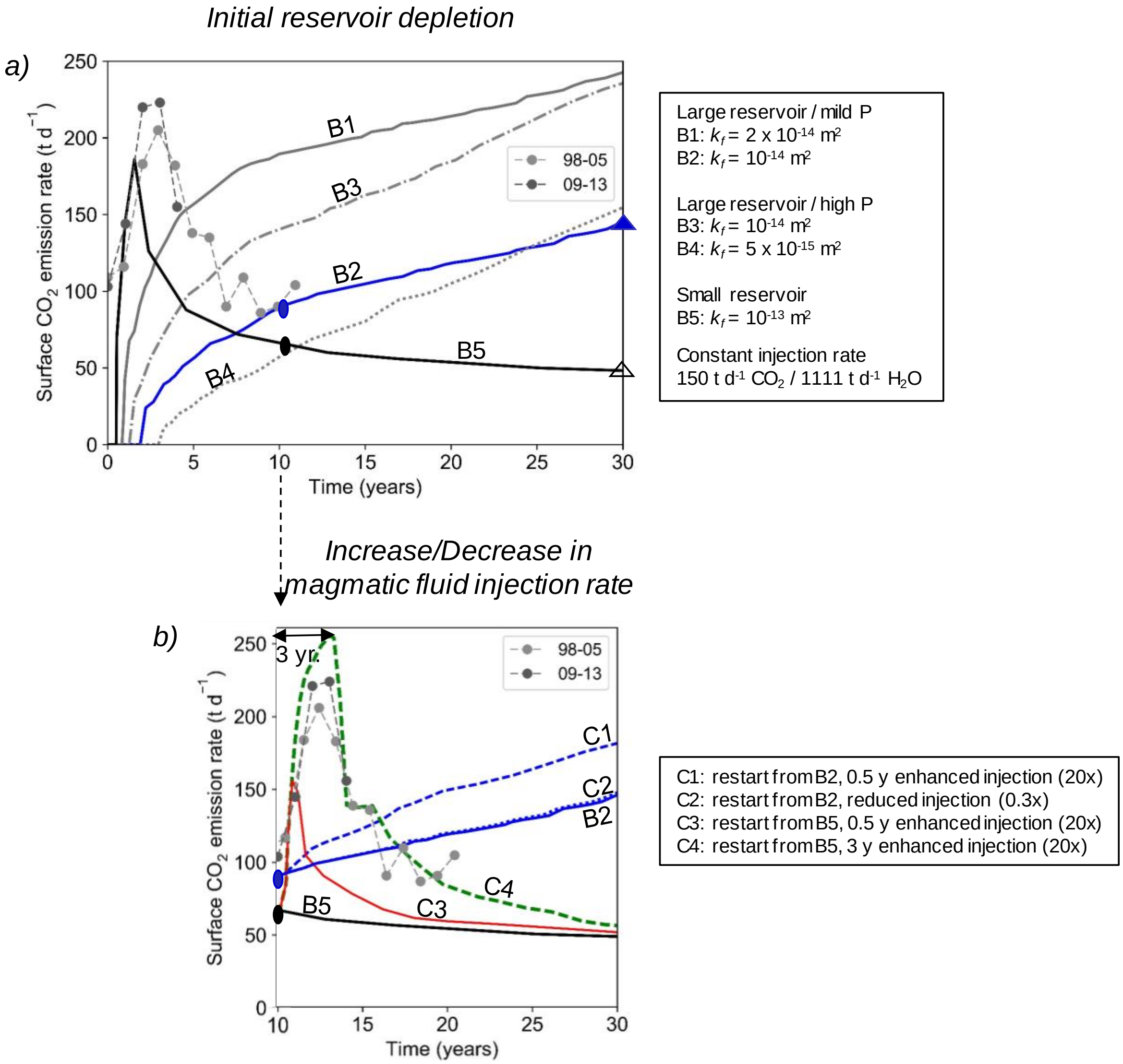

Initial reservoir depletion
a)
Surface CO2 emission rate (t d-1)
Time (years)
B1
B2
B3
B4
B5
98-05
09-13
Large reservoir / mild P
B1: kf = 2 x 10-14 m2
B2: kf = 10-14 m2
Large reservoir / high P
B3: kf = 10-14 m2
B4: kf = 5 x 10-15 m2
Small reservoir
B5: kf = 10-13 m2
Constant injection rate
150 t d-1 CO2 / 1111 t d-1 H2O
Increase/Decrease in magmatic fluid injection rate
b)
3 yr.
C1
C2
C3
C4
C1: restart from B2, 0.5 y enhanced injection (20x)
C2: restart from B2, reduced injection (0.3x)
C3: restart from B5, 0.5 y enhanced injection (20x)
C4: restart from B5, 3 y enhanced injection (20x)

Figure 6

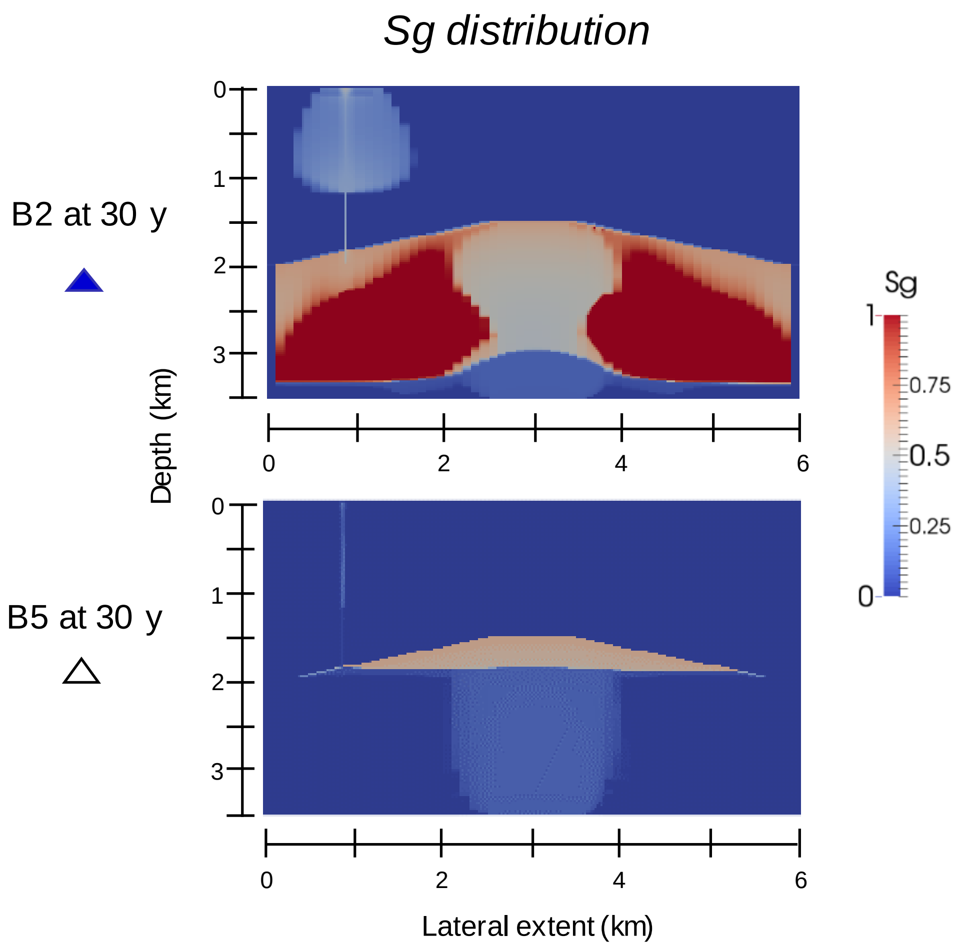
Sg distribution
B2 at 30 y
B5 at 30 y
Depth (km)
Lateral extent (km)
Sg
0
0.25
0.5
0.75
1
2
3
4
6

Figure 7

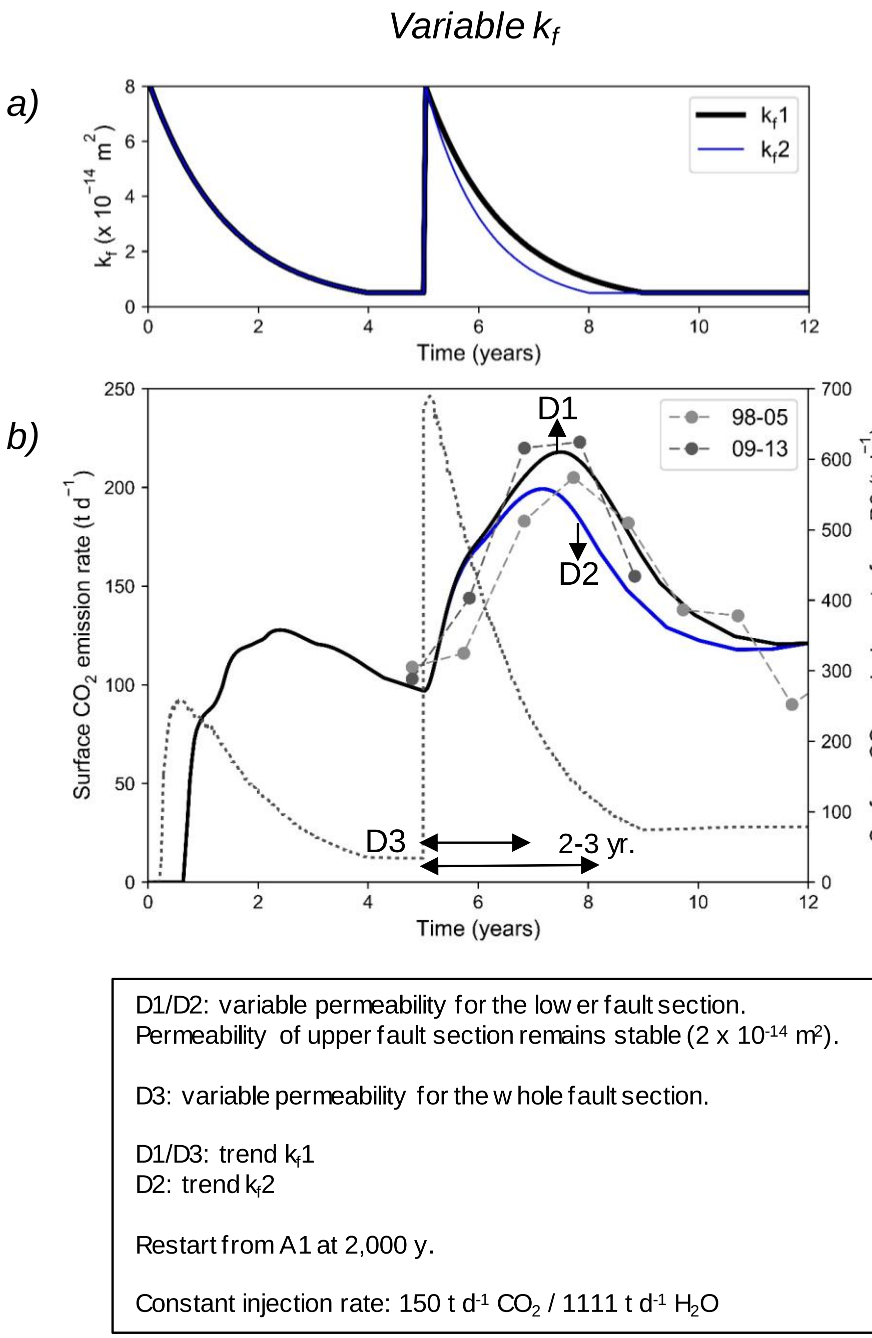

Variable k_f
a)
k_f (x 10^-14 m^2)
Time (years)
k_f1
k_f2
b)
Surface CO2 emission rate (t d^-1)
Surface CO2 emission rate from D3 (t d^-1)
Time (years)
98-05
09-13
D1
D2
D3
2-3 yr.
D1/D2: variable permeability for the lower fault section.
Permeability of upper fault section remains stable (2 x 10^-14 m^2).
D3: variable permeability for the whole fault section.
D1/D3: trend k_f1
D2: trend k_f2
Restart from A1 at 2,000 y.
Constant injection rate: 150 t d^-1 CO2 / 1111 t d^-1 H2O

Table 1

Parameter	Values	Meaning/Source
Size and geometry of modeled domain		
Length of modeled cross section (X)	6 km	Extent from south of HSL to north-west of Mammoth Mountain Fumarole (Fig. 1) .
Depth (Z)	3.5 km	Maximum gas reservoir depth (Lin, 2013).
Model width (Y)	0.5 km	A fifth of the gas reservoir width (2.5 km; Lin, 2013).
Fault location	See Figure 2	To simulate the degassing at Horseshoe Lake.
Reservoir seal	Thickness: 300 – 800 m	Arbitrary value. No published data available.
	Max. depth: 1.5 – 2 km	Based on seismic tomography (Lin, 2013).
	Dip: ~10°	To maximize reservoir domain (dischargeable CO_2-mass below Mammoth Mountain). [2]
Injection rates	150 t d^{-1} CO_2/1,111 t d^{-1} H_2O	CO_2 rate constrained by the average surface CO_2 degassing rate at HSL (Werner et al., 2014). H_2O rate allows to simulate a CO_2 content of 5.2 mol%. Higher and lower rates are investigated in simulations C.
Hydraulic properties		
Reservoir permeability, k_{res}	10^{-14} m^2	Allows convection within the reservoir (Manning and Ingebritsen, 1999). No published data available.
Seal permeability, k_{seal}	10^{-20} m^2	Impedes advective transport (Manning and Ingebritsen, 1999). No measurement available.
Fault permeability, k_f	10^{-13} – 5 x 10^{-15} m^2	Tansient fault zone permeability inferred for Mammoth Mountain (Ingebritsen and Manning, 2010).
Fault permeability decay	8x10^{-14} to 5x10^{-15} m^2 over 3-4 years	Exponential decay (Micklethwaite et al., 2016)[1]. Time period and parameters[1] allow matching CO_2 emission rates.
Shallow aquifer permeability, k_{aq}	5 x 10^{-16} m^2	[2]Limits lateral gas spreading to the degassing area observed at Horseshoe Lake.
Lower boundary permeability (k_{LB2})	10^{-16} – $10^{-18}$$m^2$	[2]Minimum permeability required for forming a gas reservoir. No published data available.
Lateral boundary permeability, k_{lb}	10^{-20} m^2	[2]Inhibits lateral fluid flow consistent with the non-thermal nature of springs surrounding the volcano (Evans et al. 2002).
Porosity	0.01	Value assigned for all domains; taken from Sorey et al. (1998).
Other properties		
Initial geothermal gradient	~70 °C/km	Corresponds to T=150°C at the reservoir top as inferred from gas geothermometry (Sorey et al., 1998).
Upper boundary temperature	10°C	To simulate air temperature.
Thermal conductivity, λ Specific heat, c_p	2.5 W m^{-1} K^{-1}/ 1000 J kg^{-1} °K^{-1}	Values assigned for all domains, taken from Todesco et al. (2010) and Wanner et al. (2014), simulating similar crystalline rocks.
Rock density, ρ	2600 kg m^{-3}	

[1] The equation describing the permeability decay of a fault damage zone over a period of N years is:

$k = k_0\, e^{-rt}$

Where k_0 (m^2) is the enhanced permeability right after the reactivation event, $k_1$is the background permeability value, k is the permeability at time t (s), and r is the decay rate computed as followed:

$$r = -\frac{1}{31{,}536{,}000\,N}\ln\frac{k_1}{k_0}$$

Values of 8 x 10^{-14} m^2 and 5 x 10^{-15} m^2 were assigned to k_0 and k_1, respectively. N was varied from 3 to 4 years.

[2]Determined from preliminary simulations

Table 2

Simulation #	Simulation period (years)	Injection rate CO_2/H_2O ($t\ d^{-1}$)	k_f (m^2)	k_{LB2} (m^2)	k_{LB3} (m^2)	INCON
Reservoir formation						
A1	2,000	150/1,111	10^{-20}	10^{-16}	10^{-16}	-
A2	2,000	150/1,111	10^{-20}	10^{-18}	10^{-20}	-
Initial reservoir depletion						
B1	30	150/1,111	2×10^{-14}	10^{-16}	10^{-16}	A1 at 2000 y
B2	30	150/1,111	10^{-14}	10^{-16}	10^{-16}	A1 at 2000 y
B3	30	150/1,111	10^{-14}	10^{-18}	10^{-20}	A2 at 2000 y
B4	30	150/1,111	5×10^{-15}	10^{-18}	10^{-20}	A2 at 2000 y
B5	30	150/1,111	10^{-13}	10^{-16}	10^{-16}	A1 at 120 y
Increase/Decrease in magmatic fluid injection rate						
C1	10-10.5 10.5-30	3,000/22,220 150/1,111	10^{-14}	10^{-18}	10^{-20}	B1 at 10 y
C2	10-30	50/370	10^{-14}	10^{-18}	10^{-20}	B1 at 10 y
C3	10-10.5 10.5-30	3,000/22,220 150/1,111	10^{-13}	10^{-16}	10^{-16}	B5 at 10 y
C4	10-13 15-30	3,000/22,220 150/1,111	10^{-13}	10^{-16}	10^{-16}	B5 at 10 y
Variable fault permeability						
D1	12	150/1,111	L: trend k_f1 / UP: 2×10^{-14}	10^{-16}	10^{-16}	A1 at 2000 y
D2	12	150/1,111	L: trend k_f2 / UP: 2×10^{-14}	10^{-16}	10^{-16}	A1 at 2000 y
D3	12	150/1,111	trend k_f1	10^{-16}	10^{-16}	A1 at 2000 y

Supplementary material for online publication only
Click here to download Supplementary material for online publication only: Supplementary Information.docx